Corrosion Science 97 (2015) 150–160

Contents lists available at ScienceDirect

Corrosion Science

journal homepage: www.elsevier.com/locate/corsci

A new combinatorial approach to assess the influence of alloy composition on the oxidation behavior and concurrent oxygen-induced phase transformations for binary Ti–*x*Cr alloys at 650 °C

Peyman Samimi [a,b,*], Yue Liu [a,b], Iman Ghamarian [a], David A. Brice [a], Peter C. Collins [a,b]

[a] Department of Materials Science and Engineering and the Center for Advanced Research and Testing, University of North Texas, Denton, TX 76203, USA
[b] Center for Advanced Non-Ferrous Structural Alloys, an NSF-I/UCRC between the University of North Texas (Denton, TX) and the Colorado School of Mines (Golden, CO), United States

ARTICLE INFO

Article history:
Received 28 November 2014
Accepted 2 May 2015
Available online 11 May 2015

Keywords:
C. Oxidation
A. Titanium
B. SEM
B. TEM

ABSTRACT

Poor oxidation performance of Ti-based alloys is an important life-limiting factor for high temperature applications. In this paper, a combinatorial approach is used to investigate systematically the influence of composition and time on the oxidation of Ti–Cr system. A compositionally graded Ti–*x*Cr specimen ($0 \leqslant x \leqslant 40$ wt%) was prepared and oxidized at 650 °C. The structure and composition of the oxide and near-surface region were studied and a critical composition of ~20 wt% Cr was identified above which the oxidation resistance is enhanced. Below the critical composition transition to a rapid breakaway oxidation was observed for extended exposure times.

1. Introduction

Poor oxidation behavior is the major barrier to the increased use of Ti-based alloys in high-temperature structural applications. The demand to increase the service temperature of these alloys beyond 550 °C (the typical temperature limit) requires careful study to understand the role that composition has on the oxidation behavior of Ti-based alloys [1–3]. The attempt to overcome this limitation in Ti-based alloys has led to the production of alloys with substantially improved oxidation resistance such as β-21S and also development of coatings and pre-oxidation techniques [1,4–6]. While it is tempting to extrapolate the oxidation behavior (e.g. oxidation rate law, depth of oxygen ingress and scale thickness) observed for a limited number of compositions under a certain oxidation condition to a broader compositional range, there are numerous examples in the literature where deviations from the expected relations are observed [7,8].

Although there have been works conducted on the oxidation behavior of Ti, such works have historically been based on traditional weight gain/loss measurements of specific engineering alloys. Surprisingly, there is a dearth of systematic studies regarding the effect of individual alloying elements on the oxidation mechanisms of Ti. Ideally, such systematic studies would not only reveal the presence of any compositional transition points in the oxidation behavior, but also reduce experimental variability. An example of such a systematic study is the combinatorial approach described in this paper and elsewhere [9] that can be used to ensure that identical testing conditions are maintained for an entire compositionally-graded specimen.

Chromium is a principal component in some metastable β Ti alloys (i.e., the burn-resistant alloys). It has been shown repeatedly that the addition of Cr to Ti (in the form of binary Ti–*x*Cr alloys) decreases the oxidation resistance. However, this observation cannot be generalized over an extended composition range of binary alloys, as it has been reported that above a certain point in the composition range, Cr is beneficial [10–12]. Interestingly, in titanium aluminides, Cr has been observed to exhibit both beneficial and detrimental results [1,13–15]. In addition to composition, the temperature and time also have an effect on the oxidation behavior, especially oxidation rate [12,16]. While the evolution of the oxidation rate for the Ti–Cr system over time and across the composition range has been reported [10], neither the associated operating mechanisms nor the change in the base material microstructure are well understood. One of the complexities associated with the oxidation behavior of the Ti–Cr system is the formation of intermetallic phase particles as a result of β decomposition (with sluggish kinetics) during the prolonged high temperature exposure. Incorporation of the intermetallic phase into the

* Corresponding author at: Department of Materials Science and Engineering and the Center for Advanced Research and Testing, University of North Texas, Denton, TX 76203, USA. Tel.: +1 817 403 4819; fax: +1 940 565 4824.
E-mail addresses: Pe.samimi@gmail.com, peymansamimi@my.unt.edu (P. Samimi).

http://dx.doi.org/10.1016/j.corsci.2015.05.002
0010-938X/

oxide scale leads to anomalous change in the oxidation rate which cannot be explained using the available theories for the high temperature oxidation of metals [8,17].

Although binary Ti–*x*Cr alloys are not used as structural materials in engineering applications, an investigation of the oxidation of this model system will provide requisite information that could then be applied to understand the oxidation behavior of more complex systems. The main goal of this study is to reveal the influence of compositional variation on the formation and evolution of the oxide scale, the subsurface microstructural evolution, and any possible deviations in the oxidation rate law.

2. Experimental procedure

High purity elemental Ti and Cr powders (Ti – 99.9% pure, −150 mesh from Alfa Aesar; Cr – 99.8% pure, plasma spray grade from Micron Metals) were used to produce a compositionally graded Ti–*x*Cr specimen ($0 \leqslant x \leqslant 40$ wt%)[1] via an Optomec LENS™ 750 at the University of North Texas. A computer-aided design (CAD) file provided a tool path for the laser deposition of a three dimensional specimen. The design file was converted and sliced into layers with a nominal thickness of 0.25 mm. The layers consisted of multiple parallel lines with a nominal hatch width of 0.38 mm. The mechanically mixed elemental powders were loaded in two independently controlled powder feeders and Ar gas was used to carry the powders into a controlled atmosphere box. A high energy Nd:YAG laser (350–500 W) provided sufficient energy for melting and in-situ alloying of the elementally blended powders under an inert Ar atmosphere. Following a line-by-line, layer-by-layer approach, a specimen was deposited onto a substrate (6 mm thick Ti–6Al–4V was used for this study) which was fixed onto a computer-controlled motorized stage. The powders were fluidized on an Ar carrier stream and injected (via four convergent Cu nozzles) into the localized melt pool created by the focused high-energy laser. The material increased the volume of the melt pool which solidified in a very rapid manner, analogous to rapid solidification processing. The pre-programmed powder flow rates allowed for the tailoring of the local composition by controlling the mass flow rates from the two powder feeders, one of them filled with pure Ti powder and the other one with mechanically mixed Ti–40Cr powder. Thus, it was possible to design and deposit a specimen with incremental variations in the composition along the length of the sample (i.e. a compositionally graded specimen). The 2D in-plane motion of the stage accompanied by vertical motion of the deposition head (including focused lens and powder nozzles) produced 3D near net shape metallic parts. The composition profile along the LENS™ deposited Ti–*x*Cr graded specimen is presented in Fig. 1. The oxygen level was maintained at a level below 20 ppm throughout the deposition and the specimen was deposited in the form of a 38 mm × 25 mm × 12 mm rectilinear solid. The compositionally graded specimen was longitudinally sectioned in individual pieces conserving the composition range.

A solution heat-treatment was carried out at above β-transus temperature for all the samples followed by water quenching (see Table 1). In order to minimize oxidation, the samples were wrapped in pure Ti foil (99.7% pure) and Ar was flowing constantly through the furnace during the solution heat-treatment to minimize oxidation. The samples were polished after solutionizing in order to expose a flat and fresh metal surface for the subsequent oxidation tests. Sample preparation included grinding with SiC abrasive papers from 120 up to 800 grit followed by polishing with 0.04 colloidal silica suspension. The samples were cleaned using a multi-step cleaning process including washes in acetone, water + surfactant and methanol.

[1] All the compositions are in wt% unless specified otherwise.

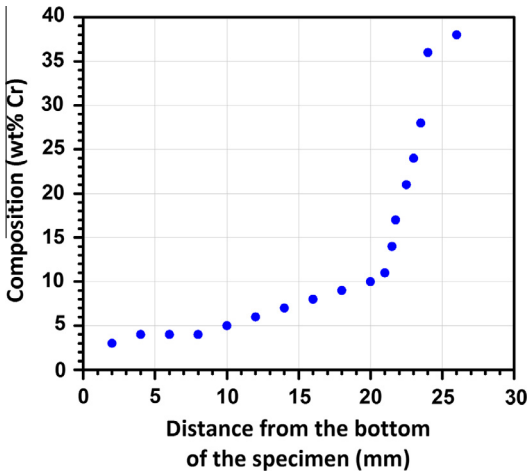

Fig. 1. Composition profile along the compositionally graded Ti–*x*Cr specimen.

Table 1
Heat-treatment and oxidation test conditions for the compositionally graded Ti–*x*Cr specimen.

Solution heat-treatment	Oxidation test
975 °C for 35 min – water quenched	650 °C for 25 h, 50 h and 100 h in still-air

The oxidation exposure conditions consisted of a temperature of 650 °C for different holding times, listed in Table 1. The samples were placed in a box furnace with the polished surface oriented upward and exposed to still laboratory-air. The samples were cut after oxidation and the cross section of the oxidized surface was polished following the aforementioned steps. Characterization of the samples, including imaging of the microstructure, elemental analysis and crystal structure studies, was conducted using a suite of electron microscopy techniques. A field emission gun (FEG) FEI™ Nova NanoSEM 230 with an integrated energy dispersive spectrometer (EDS) was used to characterize the microstructure and local composition using standardless energy EDS techniques. The results are reported to the nearest wt%. A Tecnai G2 F20 TEM operating at 200 kV accelerating voltage in both transmission electron microscopy (TEM) and scanning transmission electron microscopy (STEM) modes was employed to study the microstructural features in greater detail. Site-specific samples were prepared for TEM analysis using an FEI DualBeam™ (FIB/SEM) Nova 200 NanoLab.

PANDAT 8.1 was used for thermodynamic rationalization of the oxygen-induced subsurface microstructural transformations. PANDAT works on the basis of the CALPHAD (CALculaion of PhAse Diagrams) approach, developed for phase diagram calculation in multi-component systems [18,19].

3. Results and discussion

3.1. Microstructural evolution in the metal substrate

Backscattered SEM micrographs of four selected compositions after solution heat-treatment at 975 °C followed by water quenching are presented in Fig. 2(a–d). Considering the wide range of compositions in the graded specimen, the product phases upon quenching from the solutionizing temperature may include: α′, ω, β, β_1, β_2 and $TiCr_2$ (a Laves phase with C15 crystal structure). It should be noted that although the aim of this study is to focus

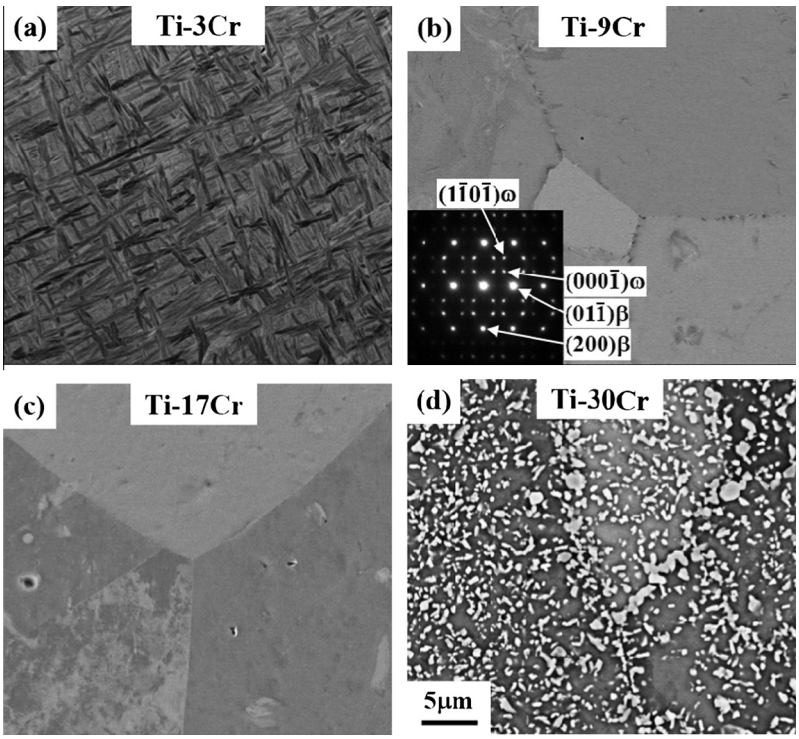

Fig. 2. Backscattered electron micrographs of (a) Ti–3Cr, (b) Ti–9Cr, (c) Ti–17Cr and (d) Ti–30Cr components after solution heat-treatment at 975 °C for 35 min followed by water quenching.

on oxidation behavior and microstructural evolution near the oxidized surface in the Ti–Cr system, the starting microstructure and different aspects of bulk phase transformation will be discussed concisely where relevant.

For low Cr concentrations, e.g. Ti–3Cr, the starting microstructure (following solutionization and water quenching) is the α′ hexagonal martensite (see Fig. 2(a)). In contrast to other commonly used β stabilizing transition metals in the commercial titanium alloys (i.e. Mo, V), the formation of the orthorhombic martensitic phase (α″) in the Ti–Cr system has not been observed [20–25]. For Ti–9Cr, the composition lies in the range where the formation of athermal ω is expected in the β matrix (see Fig. 2(b)) [20,21]. A site-specific TEM sample was prepared from the as-quenched Ti–9Cr component for the purpose of phase identification, and the corresponding selected area diffraction (SAD) pattern recorded from the specimen is shown as an inset in Fig. 2(b). The principal reflections can be consistently indexed as [0 1 1] β phase zone axis with additional reflections that arise due to the presence of fine-scale athermal ω particles. Although there is no general agreement in the literature on the beginning and ending compositions of ω formation in the Ti–Cr system, 17 wt% Cr is beyond all the reported values, thus 100% β retention is expected for this composition (see Fig. 2(c)). Solution heat-treatment at 975 °C for compositions exceeding ~25 wt% Cr corresponds to a composition/temperature combination that lies within the α + $TiCr_2$ two phase-field region, owing to the high solvus temperature of the intermetallic phase (~1220 °C) [26]. Therefore, the presence of the pre-existing Laves phase particles in the β matrix of the as-quenched microstructure is expected and is shown in Fig. 2(d).

Fig. 3(a–c) shows backscattered SEM micrographs of the subsurface microstructure of a Ti–3Cr component oxidized at 650 °C for 25, 50 and 100 h. During the isothermal oxidation experiment, the martensitic phase (α′) has decomposed to various product phases described in the next paragraph, including β, α and $TiCr_2$. It is noted that for the material located very close to the surface, there is local oxygen enrichment prior to the formation of a stable surface oxide, and such enrichment could (and does, as will be shown) change the transformation kinetics and lead to different microstructural morphologies compared to the bulk.

The equilibrium eutectoid reaction in the Ti–Cr system, βTi → αTi + $TiCr_2$, occurs at ~667 °C [3,21,27]. Thus, the precipitation of the $TiCr_2$ phase is expected to be observed during isothermal holds at 650 °C. However due to the sluggish nature of this reaction, the formation of the intermetallic phase is not observed generally for chromium levels below 5 wt% Cr at service temperatures [3,20,21,28]. From Fig. 3(a) it is immediately apparent that after 25 h oxidation, although at a temperature and composition within the α + $TiCr_2$ two-phase region, the decomposition of α′ in the bulk has resulted in an α + β microstructure, with the metastable β phase present at the prior martensite lath boundaries and defects (i.e. dislocations and twins). It is only in the region close to the oxidized surface where the precipitation of nascent $TiCr_2$ particles was observed. This can be attributed to the higher rate of β decomposition in the presence of interstitial elements such as O, as has been reported by Molchanova [23]. After 50 h oxidation however the formation of $TiCr_2$ particles was not limited to regions in close proximity to the surface, as the diffusion of oxygen along the grain boundaries of the prior β grains resulted in the intergranular precipitation of the intermetallic phases (see Fig. 3(b)). After the 100 h oxidation exposure, the metastable β phase has had sufficient time to decompose into α + $TiCr_2$ and the microstructure shows a uniform distribution of $TiCr_2$ particles surrounded by the α phase (see Fig. 3(c)).

In order to determine the degree of β decomposition after 100 h and to compare the results with those expected for the equilibrium condition, the area fraction of the Laves phase particles in Fig. 3(c) was quantified by manual thresholding and subsequent areal analysis. The results are provided in Table 2. In the backscattered SEM micrographs, the $TiCr_2$ particles can be identified easily as they appear brighter relative to both the α and β phases, due to the

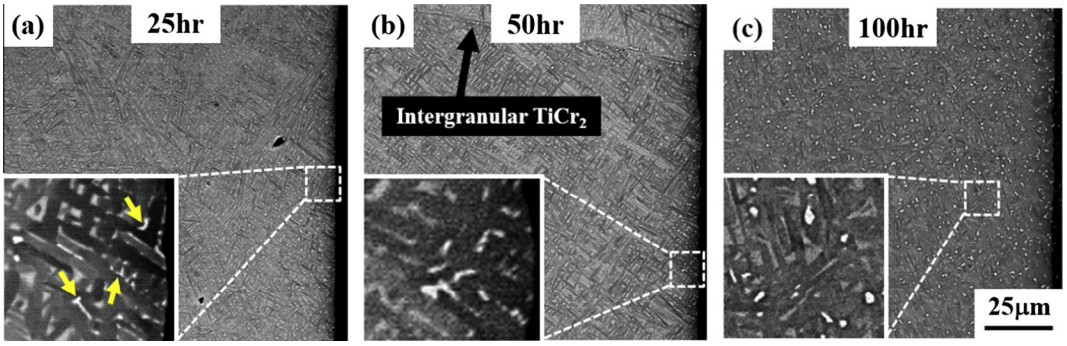

Fig. 3. Backscattered electron micrographs of the subsurface microstructure of Ti–3Cr component oxidized at 650 °C for (a) 25, (b) 50 and (c) 100 h.

Table 2
Experimentally measured area fraction and calculated equilibrium volume fraction of $TiCr_2$ phase in three selected compositions for different holding times.

Composition	Oxidation time (h)	Area fraction (%) (experimental)	β Decomposition completion (%)	Volume fraction (%) (calculated by PANDAT)
Ti–3Cr	100	1.59	44.28	3.59
Ti–9Cr	25	2.80	22.54	
Ti–9Cr	50	2.81	22.62	12.42
Ti–9Cr	100	8.08	65.06	
Ti–17Cr	25	21.18	87.07	
Ti–17Cr	50	25.09	103.166	24.32
Ti–17Cr	100	25.01	102.85	

higher average atomic number. This clear distinction is essential for faithful thresholding and subsequent quantification [29]. For Ti–3Cr, the measured result was ~1.6% area fraction for the Laves phase after 100 h at 650 °C, which deviates from the equilibrium volume fraction of $TiCr_2$ predicted using PANDAT 8.1 (~3.6% (see Table 2)). The comparison of the experimental and calculated values revealed that roughly ~44% of the predicted β decomposition has taken place after 100 h oxidation, assuming that nucleation of $TiCr_2$ is not a direct product of martensite decomposition and proceeds following an intermediate step (Eq. (1)):

$$\alpha' \rightarrow \alpha + \beta \rightarrow \alpha + \beta + TiCr_2 \quad (1)$$

For an alloy content of Ti–9Cr, a considerable increase in the volume fraction of metastable β was observed after 25 and 50 h oxidation (see Fig. 4(a and b)) which is expected considering the strong β stabilizing effect of Cr. The heterogeneous precipitation of Laves phase particles along the grain boundaries of the prior β grains (in a seemingly continuous fashion at some boundaries), α interfaces and in the regions close to the surface is observed. Following exposure to laboratory air at 650 °C for 100 h, a uniform intragranular distribution of $TiCr_2$ particles is observed for Ti–9Cr (see Fig. 4(c)).

The results of the microstructure quantification for the micrographs presented in Fig. 4(a–c) are given in Table 2, with the percent β decomposition reported with respect to the predicted equilibrium volume fraction of $TiCr_2$, as calculated by PANDAT. Somewhat surprisingly, for the Ti–9Cr composition, it can be seen that the same degree of β decomposition (~22%) exists after both 25 and 50 h. After 100 h ~65% of the decomposition reaction has occurred.

For a hypereutectoid alloy composition of Ti–17Cr, there is not a considerable difference between the microstructures after the various exposure times (i.e., 25–100 h) except for the presence of a few β islands in the 25 h oxidized sample which decompose with the passage of time (see Fig. 5(a–c)). Also observed is an extensive precipitation of $TiCr_2$ particles as well as the refinement and development of a fine scale lamellar structure which occurs, notably, at only some of the prior β grain boundaries as a product of cooperative growth. The results of the microstructural quantification of the region corresponding to a composition of Ti–17Cr are given in Table 2. There is an unexpected result with respect to the percent β decomposition, which exceeds 100% for 50 and 100 h oxidation times. This can be attributed to two possible sources. Firstly, there is an experimental uncertainty associated with the image processing (i.e. thresholding) and stereological measurements. Given the considerable variation in the size of the Laves phase particles in the regions in a close proximity to the boundaries of the prior β grains, it is reasonable to expect a ±1% uncertainty in the measurement, as observed in other Ti-based alloys [29]. The second is the effect of O, which decreases the solubility of Cr in the α-phase, potentially increasing the volume fraction of $TiCr_2$ particles. Together, these are responsible for the seemingly inexplicable >100% β decomposition completion values in Table 2. It was previously shown by the authors that the depth of oxygen diffusion along the grain boundaries (fast diffusion pathways), from the exposed surface in a binary Ti-based system, can extend up to 500 μm [9]. The faster kinetics of beta decomposition in the presence of oxygen around the grain boundaries leads to the abovementioned size variation which in turn increases the probability of thresholding errors. When the results of the microstructural quantification for the Ti–3Cr, Ti–9Cr and Ti–17Cr compositions, as reported in Table 2, are compared, the strong influence of composition on the kinetics of the β decomposition reaction and the role of the exposure time become evident. Not surprisingly, it can be concluded that for a certain holding time a larger portion of β phase decomposes to $\alpha + TiCr_2$ as the Cr content increases.

It should be noted that although the Ti–Cr system is a β-eutectoid system, no evidence of the formation of the pearlitic or lamellar structure is observed upon cooling from above the eutectoid temperature except for hypereutectoid alloys when a large undercooling is applied and the predominant mode of eutectoid decomposition is bainitic or non-lamellar [21,30–34]. Although the intermetallic phase particles have detrimental effects on the mechanical properties that make them undesirable in high temperature commercial Ti alloys for bulk structural applications, its impact on the oxidation behavior of the Ti–Cr system is the reason that authors highlighted the evolution of this phase.

3.2. Oxide scale

Fig. 6(a–c) shows backscattered SEM micrographs of the oxide layer in cross-section for the three selected compositions discussed previously after 25 h oxidation at 650 °C. Due to the notable difference in the average atomic weight of the oxide and the base

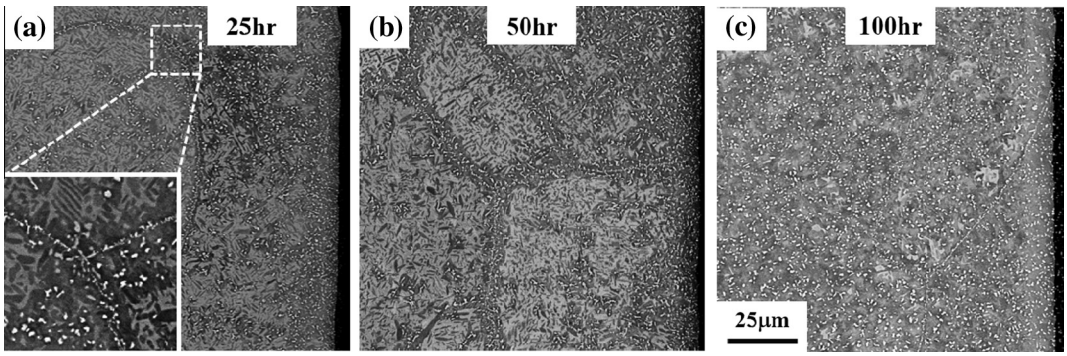

Fig. 4. Backscattered electron micrographs of the subsurface microstructure of Ti–9Cr components oxidized at 650 °C for (a) 25, (b) 50 and (c) 100 h.

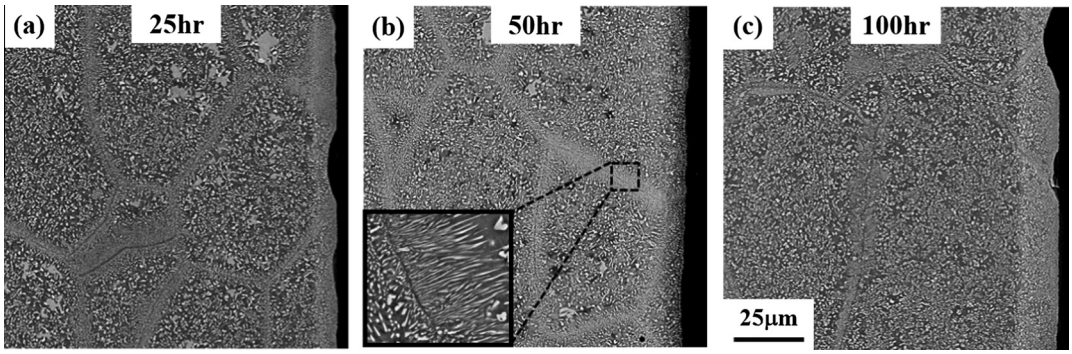

Fig. 5. Backscattered electron micrographs of the region just below the surface of Ti–17Cr components oxidized at 650 °C for (a) 25, (b) 50 and (c) 100 h.

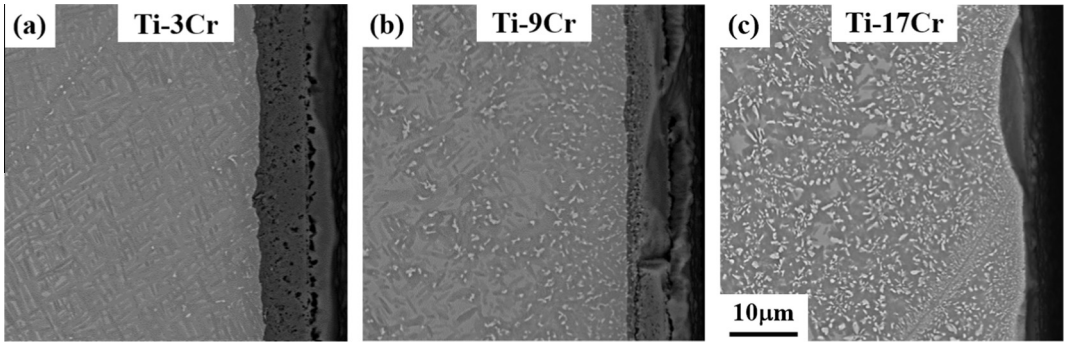

Fig. 6. Backscattered electron micrographs of the oxide layer in cross-section for (a) Ti–3Cr, (b) Ti–9Cr and (c) Ti–17Cr components after 25 h oxidation at 650 °C.

material, the imaging conditions (i.e. brightness and contrast) were adjusted in order to capture both the metal substrate and the oxide scale. The effect of composition on the scale thickness is clearly evident as the relatively thick multi-layer oxide scale for the region corresponding to a composition of Ti–3Cr is replaced by a thin, barely visible single layer scale for the region corresponding to a composition of Ti–17Cr. The variations of the scale thickness as a function of composition for the entire composition range for 25, 50 and 100 h is shown in Fig. 7.[2] The thickness values are averaged over 6 independent measurements for each nominal composition. It is evident that for a certain composition range (i.e., 0–20%), the formation and growth of the oxide scale on the metal surface is strongly dependent on the composition and, to a lesser degree, the holding time. For an oxidation exposure time of 25 h, the thickness of the oxide scale gradually decreases (from ~11 μm to ~1 μm) as the concentration of Cr increases to ~20 wt% Cr. For the case of 50 h oxidation there is a slight upward shift of the graph compared to 25 h oxidation, and a similar variation in the thickness of the scale with respect to the composition. Interestingly, this relative stability in oxide scale thickness mirrors the relative stability in the volume fraction of the $TiCr_2$ phase in the base material for both Ti–3Cr and Ti–9Cr, as reported in Table 2. As the holding time is extended to 100 h there appears a significant increase in the scale thickness and the trend has a steeper slope. However, for compositions above ~20 wt% Cr, there is virtually no difference in the thickness of the oxide layer. Since there is a drastic difference in the oxidation behavior above and below this seemingly critical content of Cr (~20 wt%), the composition ranges above 20 wt% and below 20 wt% will be discussed separately.

In order to understand the role of kinetics on the evolution of the oxide scale, the data of scale thickness as a function of oxidation time has been plotted (see Fig. 8) for selected compositions. It is well-established that the oxidation kinetics of Ti at 650 °C can be explained by a parabolic rate law [1,6,35–42] which can be described, in its simplest form, according to Eq. (2):

[2] For the sake of visibility of the data points that read close to zero, the y axis is split by a break in some of the plots.

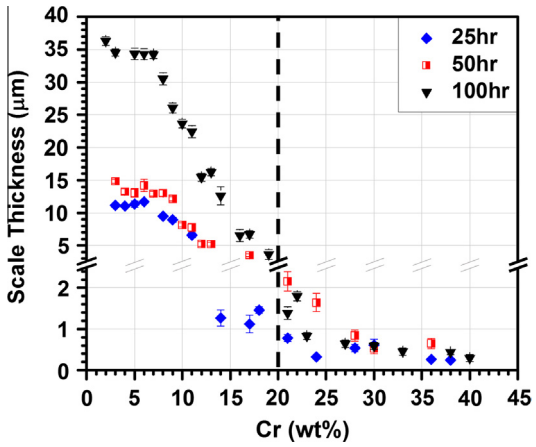

Fig. 7. Scale thickness versus Cr content for binary Ti–Cr systems oxidized for 25, 50 and 100 h at 650 °C.

$$X^2 = k_p t \tag{2}$$

and the parabolic oxidation rate can then be expressed according to Eq. (3):

$$\frac{dX}{dt} = \frac{k'_p}{X} \tag{3}$$

where k_p is parabolic rate constant, t is the oxidation exposure time and X represents any measurable quantity that is directly proportional to the extent of oxidation reaction such as weight gain or scale thickness. The parabolic rate constant k_p is factor that includes several parameters, including temperature, oxygen partial pressure, charge and flux of mobile ionic species, chemical potential gradient and any operable short-circuit diffusion mechanism. According to Wagner's theory of oxidation, developed for thick oxide films (~1 μm<) and which predicts the kinetics based on parabolic growth, the oxidation rate gradually decreases with the passage of time [17,43,44]. Surprisingly, the plots shown in Fig. 8 for the nominal compositions of 3, 6, 8, 11 and 17 wt% Cr do not follow the expected parabolic rate law and the results indicate the occurrence of a rapid breakaway oxidation. It is worth mentioning that the investigations concerning the oxidation of these alloys are unfortunately more or less in agreement in concluding that the oxidation resistance of the titanium decreases markedly after the addition of chromium [45,46]. However above a critical composition (i.e., ~Ti–20Cr in Fig. 7), the binary components appear to be very

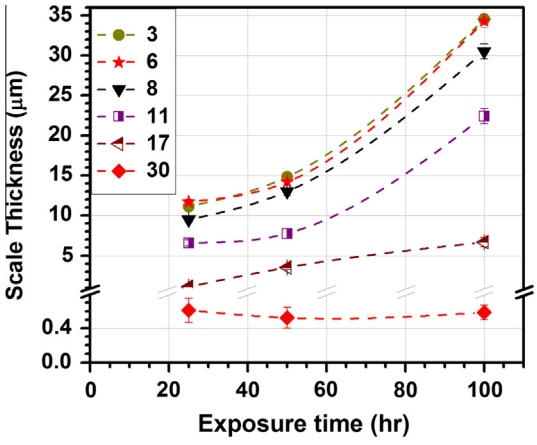

Fig. 8. Scale thickness as a function of exposure time for six selected Ti–Cr components oxidized at 650 °C.

resistant to oxidation at 650 °C. In order to explain this unusual behavior, the concurrent microstructural evolution of the oxide scale and the metal substrate must be considered.

Two different mechanisms can be proposed for the rapid breakaway oxidation reaction for low Cr contents. The first mechanism is the cracking of the scale due to the stresses associated with the isothermal growth of the scale, resulting in the formation of micro-cracks in the oxide layer. These micro-cracks act to supply continuously oxygen to the base material and result in the local transition from diffusion-controlled to reaction-controlled oxidation and consequently an acceleration of the reaction. The second proposed mechanism involves only ionic diffusion across the oxide layer, thus is a fully diffusion-controlled mechanism. In order to identify the predominant mode of oxidation it is necessary to fully characterize the oxide scale and the metal substrate.

A backscattered SEM micrograph of the cross-section microstructure of a composition of Ti–10Cr after exposure to laboratory air at 650 °C for 100 h is shown in Fig. 9(a). The structure, morphology and phase variation across the oxide scale and into the metal substrate are discussed below. The oxide scale can be divided into three layers (parallel to the metal/oxide interface) based on the continuity of the scale. The outermost layer, referred to as layer 1 (L1), is compact with no microporosity, and has largely delaminated from the second layer, though the connection is preserved at some locations, preventing spallation. The middle layer, layer 2 (L2), is relatively thin, while layer 3 (L3) is the thickest layer of the oxide scales. Layer 3 exhibits a porous structure, and terminates at the metal/oxide interface. The formation sequence and growth direction of the three oxide layers are determined by the type and disorder of the oxide. Titanium oxide is an n-type oxide in which the predominant type of disorder could be either non-metal deficit or metal excess, depending upon the oxygen pressure and temperature [1,47]. Accordingly, the oxidation reaction progresses with the inward migration of oxygen anions and the metal/oxide interface is considered to be the oxidation front. Thus, L1 is the first layer that forms on the metal surface, followed by the formation of L2 and L3. Notably, it can be seen that the Laves phase particles do not immediately undergo a phase transformation as the oxidation front passes. Rather, they gradually dissolve within the oxide as the oxidation reaction proceeds and act as sources of Cr ions for the enrichment and modification of the scale. Fig. 9(b) is a STEM micrograph recorded from the metal/oxide interface of a Ti–11Cr component after 25 h oxidation and clearly shows the existence of $TiCr_2$ particles on both sides of the oxidation front (i.e., base metal/oxide scale interface).

The X-ray diffraction (XRD) pattern acquired from the oxide surface corresponding to a composition of ~3–4 wt% Cr after 25 h oxidation is given in Fig. 10. There appears to exist only one phase which has been indexed as rutile TiO_2 with the experimentally measured lattice parameters of $a = 4.586$ Å and $c = 2.961$ Å, which is in very good agreement with the expected rutile structure and lattice parameters (4.584 Å and 2.954 Å). The XRD data from the oxide surface of a region corresponding to ~9–10 wt% Cr showed that TiO_2 lattice parameters are identical to the Ti–3Cr composition (i.e., $a = 4.586$ Å and $c = 2.961$ Å) which indicates that Cr content does not influence the Ti oxide lattice constants in the topmost oxide layer (L1). This is expected when considering the similar ionic radii of Ti^{4+} (0.61 Å) and Cr^{3+} (0.62 Å) in octahedral coordination [48]. However, as XRD is a surface sensitive technique, it can be used to identify only the phases present in L1. Therefore, TEM analysis is required for the full characterization of all of the layers within the oxide scale. A site-specific TEM sample was prepared using the DualBeam™ FIB/SEM from a location with the nominal composition of Ti–11Cr after 25 h oxidation at 650 °C. A many-beam bright field micrograph of the Ti–11Cr component is shown in Fig. 11(a) in which, the metal substrate, L1, L2, L3 and

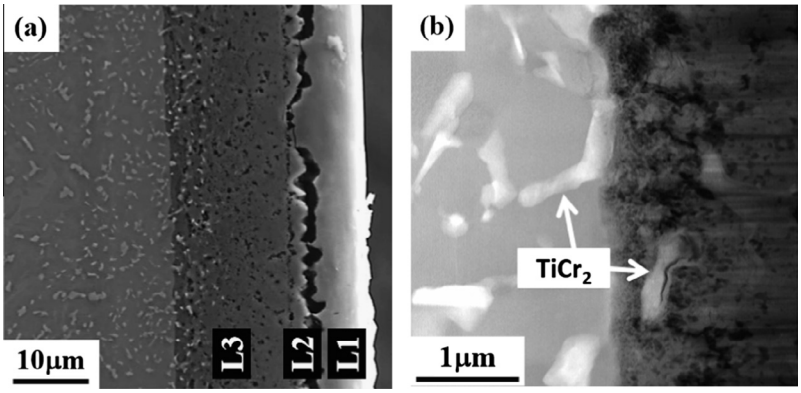

Fig. 9. (a) Backscattered electron micrograph of the cross-section microstructure of a Ti–10Cr component after100 h oxidation and (b) a STEM micrograph recorded from the metal/oxide interface of a Ti–11Cr component after 25 h oxidation.

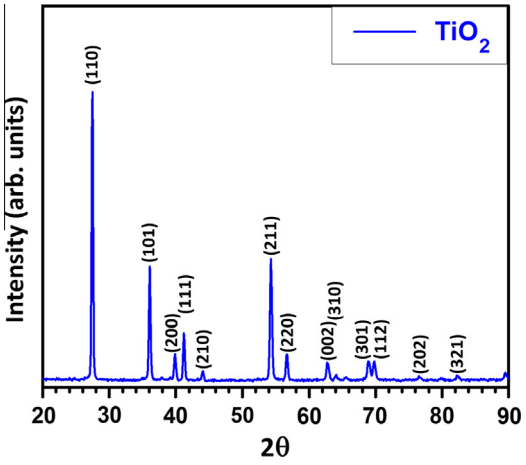

Fig. 10. The X-ray diffraction pattern acquired from the oxide surface of a region corresponding to a composition of ~3–4 wt% Cr after 25 h oxidation at 650 °C.

the protective Pt layer are labeled and separated by dashed lines. It should be noted that the oxide scale was milled away at some locations while thinning using the focused ion beam due to its porous structure. However, it is not expected to significantly affect the TEM analysis since all the layers in the specimen contained a sufficiently large area to analyze. It is clearly evident in Fig. 11(b) that there is a considerable variation in the grain size across the oxide layer interfaces and the size reduces from L1 to L2 to L3 respectively (2–3 μm in L1, 0.5–1 μm in L2 and ⩽0.1 μm in L3).

Three SAD patterns obtained from L2, L2/L3 interface and L3 are presented in Fig. 11(c–e). The SAD pattern in Fig. 11(c) corresponds to the [0 0 1] zone axis of rutile. Extra reflections arising from multiple grains are visible as the region of SAD analysis transitions to the L2/L3 interface (see Fig. 11(d)). Within layer 3 (L3), immediately below the L2/L3 interface (i.e., avoiding regions where the $TiCr_2$ Laves phase particles are stable) the diffraction pattern exhibits a larger number of extra spots (see Fig. 11(e)) due to grain refinement. Accurate d-spacing measurement of the extra reflections in Fig. 11(e) revealed that they correspond to the rutile structure. This indicates that although the size of the grains change, there is no change in crystal structure. The same method was applied across L1/L2 interface and the results indicate only single-phase rutile. The TEM and XRD are self-consistent. Rutile is the only crystal structure present in L1, L1/L2 interface, L2, L2/L3 interface and just below L2/L3 interface. Contrary to competing hypotheses [11,12], there is no evidence of the formation of a new oxide (Cr_2O_3) within TiO_2.

The size variation across the oxide layer interfaces can be attributed to the formation of these layers at different stages of the oxidation reaction and sintering/coarsening of the oxide crystals formed during the earliest stages of the prolonged high temperature exposure.

Fig. 12(a and b) shows a bright-field TEM micrograph and the corresponding STEM–EDS Cr concentration map that spans across the three oxide layers as well as a small portion of base metal from the Ti–11Cr composition after 25 h oxidation at 650 °C. These observations are in agreement with the conclusion drawn from the XRD and diffraction pattern study, as no Cr-rich phase was found in L1, L2 and the top portion of L3, thus indicating a compositionally homogeneous, rather than heterogeneous, oxide scale. However there exists a distribution of Cr rich particles that extends from ~300 nm below the L2/L3 interface into the metal substrate. Elemental analysis of these Cr rich regions showed that they all contain a level of Ti consistent with $TiCr_2$ which further disproves the hypothesis of the formation of a new oxide (Cr_2O_3) within TiO_2 as a result of dissolution of $TiCr_2$ particles.

The Ti, Cr and O content of eight particles has been measured, and is plotted as function of distance from the metal/oxide interface (see Fig. 12(d)). The intermetallic phase exhibits a near stoichiometric composition of $TiCr_2$ in the metal substrate and significantly deviates deeper into the oxide scale, indicating that dissolution rate of $TiCr_2$ phase is less than oxidation rate of Ti. Some of the partially dissolved $TiCr_2$ particles are shown in the STEM image in Fig. 12(c).

The Cr atoms, driven out of the Laves phase during the gradual dissolution in TiO_2 form a highly doped oxide. Site occupancy of the Cr ions is the key factor that can alter the oxidation rate from a parabolic trend for pure Ti to an unexpected exponential trend. Cr ions can occupy both substitutional and interstitial cation sites in TiO_2 structure and the reaction equations can be written as Eqs. (4) and (5):

$$TiCr_2 \rightarrow 2Cr_{Ti}^{-} + V_O^{++} + Ti_{Ti} \quad (4)$$

$$TiCr_2 \rightarrow 2Cr_i^{+++} + 6e^{-} + Ti_{Ti} \quad (5)$$

where Cr_{Ti} is a Cr ion that occupies a Ti site (substitutional cation), Cr_i is an interstitial Cr ion; V_O is an oxygen vacancy; and Ti_{Ti} is a normal Ti ion in TiO_2 lattice. It should be noted that Ti ions can also occupy interstitial sites. However, at atmospheric pressures, the oxygen vacancy is the dominant type of point defect in TiO_2 [47]. While it is not possible to unequivocally determine whether dissolution of Cr ions is predominantly substitutional or interstitial based upon the experimental results provided in this paper, nevertheless, the influence of the type of site on the oxidation rate variation can be discussed.

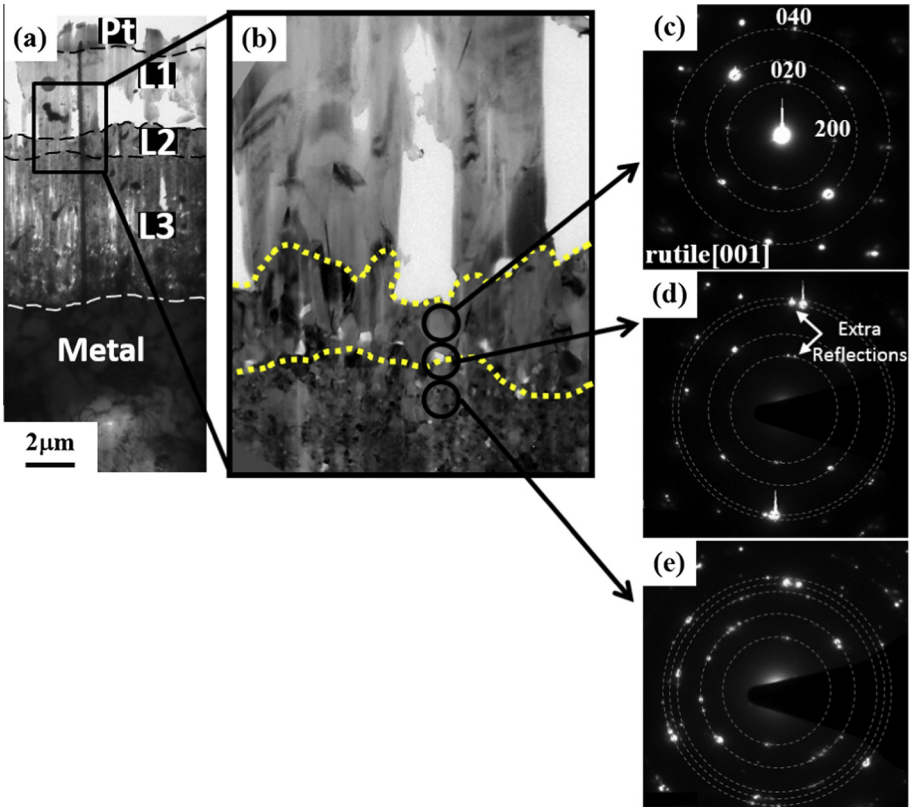

Fig. 11. (a and b) Many-beam bright field TEM micrographs of the metal/oxide interface of a Ti–11Cr component oxidized for 25 h and (c–e) the corresponding SAD patterns recorded from the marked regions.

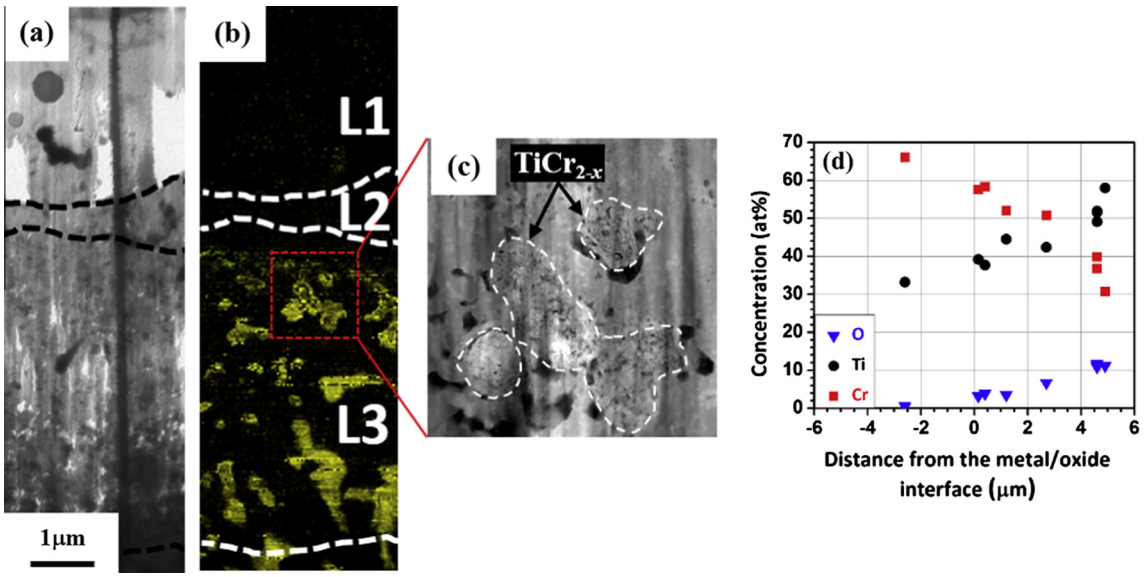

Fig. 12. (a–c) Bright-field TEM micrograph, the corresponding STEM–EDS Cr concentration map and STEM micrograph recorded from a Ti–11Cr composition after 25 h oxidation at 650 °C. (d) Composition of the $TiCr_2$ particles as a function of distance from the metal/oxide interface.

The Cr cations (Eq. (4)) with a lower valence than that of Ti cations carry an effective negative charge if they occupy substitutional sites when dissolved in TiO_2. This is accompanied by the formation of half as many oxygen vacancies in order to maintain the charge neutrality. For the case of interstitial Cr cations (Eq. (5)) the effective charge would be positive and the number of oxygen vacancies decreases as a result of doping with Cr. When considering the inward migration of oxygen ions as the oxidation mechanism of Ti alloys, the substitutional dissolution of Cr in TiO_2 will have a detrimental effect on the oxidation resistance of the alloy as it increases the bulk diffusion coefficient via providing more oxygen vacancies.

The abovementioned phase evolution in the oxide scale supports the second mechanism proposed earlier in this paper (i.e., the diffusion-controlled oxidation reaction involving ionic migration across the oxide scale), leading to the breakaway oxidation

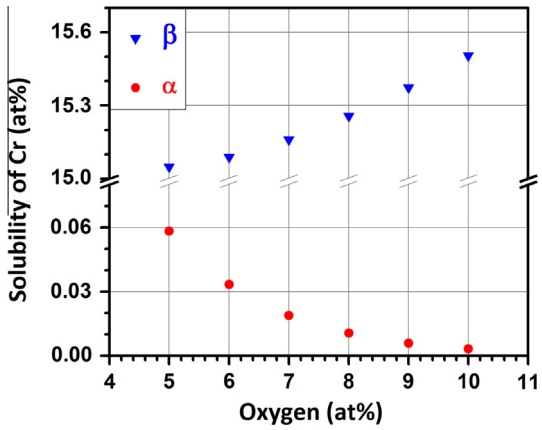

Fig. 13. Chromium solubility of a phase as a function of oxygen concentration for a Ti–5Cr composition predicted by PANDAT for the equilibrium condition at 650 °C.

reaction for Cr contents below ~20 wt%. As was shown in Fig. 2(a–c), there were no pre-existing $TiCr_2$ particles in the as quenched alloys with the Cr concentration below 17 wt% Cr. The first Laves phase particles (specifically for the low Cr components) form in close proximity to the surface as a result of Cr depletion of the α phase which is enriched with oxygen. The ingress of oxygen during oxidation decreases the Cr solubility of α phase (see Fig. 13). Consequently, the Cr atoms diffuse toward the bulk as the oxidation front advances into the metal substrate. Above a critical concentration the first Laves phase particles precipitate in the Cr rich β phase near the oxidized surface. Although the oxidation resistance of $TiCr_2$ phase is substantially higher than Ti, the volume fraction of this phase is not sufficiently large so as to decrease the overall oxidation rate. The dissolution of the $TiCr_2$ phase in the oxide scale is a function of oxidation time, as is the number of oxygen vacancies and consequently, the oxidation resistance. According to Fig. 7, for low Cr compositions it can be concluded that oxidations times of 25 and 50 h are not long enough for the $TiCr_2$ particles to become trapped and completely dissolved in TiO_2. However, after 100 h a large number of these particles have reacted and formed a TiO_2 scale that is heavily doped with Cr. This mechanism is clearly depicted in Fig. 14a–c, showing a backscattered electron micrograph and the associated EDS O and Cr concentration maps recorded from the oxide scale of a Ti–10Cr component after 100 h oxidation. According to Fig. 14 the porous oxide (the bottom layer) contains a high density of Cr rich regions (i.e. gradually dissolving Laves phase particles) and the top layer is also doped with the dissolved Cr ions, unlike the Cr distribution map after 25 h oxidation for Ti–11Cr component (Fig. 12b), which emphasize on the time dependency of the rapid breakaway oxidation phenomenon. The concurrent loss of Cr ions through evaporation from the oxide surface is also expected, considering the extent of Cr incorporation into the titanium oxide [49].

Substitution of Ti ions with Cr ions thus, degrades the oxidation resistance via increasing the inward flux of oxygen in an extrinsic regime and is considered to be the dominant mechanism responsible for the unusual rapid breakaway oxidation reaction.

For the compositions above 20 wt% Cr however, following the initial stages of oxidation the volume fraction of the Laves phase

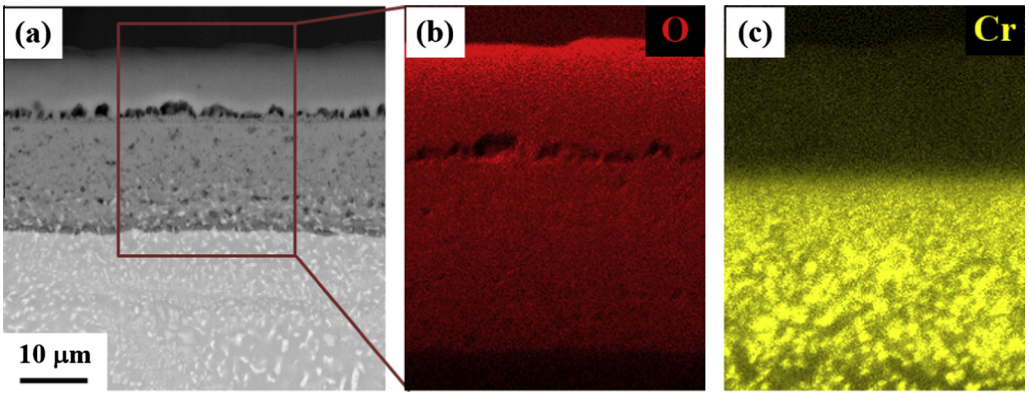

Fig. 14. (a–c) Backscattered electron micrograph and the associated EDS O and Cr concentration maps recorded from the oxide scale of a Ti–10Cr composition after 100 h oxidation at 650 °C.

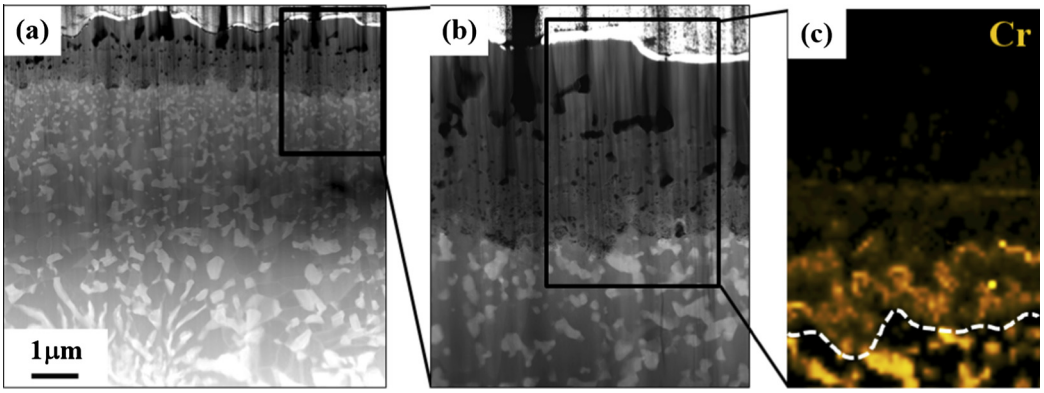

Fig. 15. (a and b) The STEM micrographs of the cross-section morphology of a Ti–24Cr composition oxidized for 25 h at 650 °C and (c) the corresponding STEM–EDS Cr concentration map.

near the surface, including both the pre-existing and oxidation-induced $TiCr_2$ particles, is quite high, as illustrated in Fig. 15(a and b) which shows STEM micrographs of the cross-section morphology of a Ti–24Cr component oxidized for 25 h. Laves phase particles show a noticeable size variation ranging from $\leqslant$200 nm at just below the metal/oxide interface to $\geqslant$200–300 nm at 6 μm distance from the interface. The concurrent ingress of oxygen and decomposition of the supersaturated β phase is responsible for this size variation, considering the absence of pre-existing $TiCr_2$ particles after solution heat-treatment for this composition. The high volume fraction of $TiCr_2$ particles which are characterized by a remarkable oxidation resistance on both sides of the metal/oxide interface (see Fig. 14(c)) act as a barrier to diffusion of oxygen and compensate the detrimental effect of Cr ions in TiO_2 oxide leading to the improved overall oxidation resistance.

The SEM and TEM observations of the oxide scale did not show any indication of the formation or propagation of micro-cracks that penetrate the oxide scale and expose the fresh metal surface to atmosphere. Thus, the oxygen ingress is due to diffusion through the oxide scale.

4. Conclusions

A compositionally graded Ti–*x*Cr specimen (produced by LENS™) was used to systematically assess the oxidation behavior of binary Ti–Cr system as a function of composition and exposure time including formation and evolution of the oxide scale and the metal substrate, effect of oxygen ingress, operating oxidation mechanisms and transition in the oxidation rate. The following salient observations and conclusions are drawn:

1. For regions close to the surface, oxygen enrichment of the base material, prior to the oxide formation, changes the transformation kinetics and stabilizes $TiCr_2$ particles for unusually low solute levels (e.g., Ti–3Cr).
2. There is also a critical concentration (~20 wt% Cr) above which the oxidation resistance is significantly increased and the scale thickness becomes more or less unresponsive to the time and concentration variations.
3. The $TiCr_2$ Laves phase particles do not immediately transform as the oxidation front passes. Rather, the particles gradually dissolve within the oxide and act as sources of Cr ions which enrich the scale, yet do not change the nature of the oxide or its lattice parameters. As the Cr cations exhibit a lower valence than that of Ti cations, carry an effective negative charge in form of substitutional impurities in TiO_2 therefore the concentration of oxygen vacancies is increased in order to maintain the charge neutrality. This is the most probable mechanism impacting the inward migration of oxygen ions. However the exposure time must be long enough for the $TiCr_2$ particles to form, become trapped and dissolve in the scale to reveal the detrimental effect of substitutional Cr ions.
4. As this is a time dependent process, an oxidation time of 100 h is long enough to form an oxide scale, heavily doped with Cr which is considered to be responsible for deviation from the expected parabolic rate law and occurrence of a rapid breakaway oxidation for Cr contents below critical concentration.
5. For the compositions above the critical Cr content the alloys can benefit from the remarkable oxidation resistance of the Laves phase particles since the volume fraction of this phase is large enough to improve the overall oxidation resistance.
6. The oxide scale of the Ti–*x*Cr components ($x < \sim$20 wt%) consists of three layers L1–L3. Rutile is the only phase present in L1, L1/L2 interface, L2, L2/L3 interface and just below L2/L3 interface while the rest of L3 is a mixture of TiO_2 and partially dissolved $TiCr_2$ particles.

Acknowledgements

This work was conducted within the NSF I/UCRC Center for Advanced Non-Ferrous Structural Alloys (CANFSA) which is a joint industry-university center between the Colorado School of Mines and the University of North Texas. The authors gratefully acknowledge the support of NSF (Award Number 1134873) and the support and active mentorship of the industrial partners. The authors also gratefully acknowledge the facilities available at the University of North Texas' Center for Advanced Research and Technology (CART).

References

[1] C. Leyens, M. Peters, Titanium and Titanium Alloys, Wiley, 2006.
[2] R. Boyer, An overview on the use of titanium in the aerospace industry, Mater. Sci. Eng. A 213 (1996) 103–114.
[3] G. Lütjering, J.C. Williams, Titanium, Springer, 2007.
[4] H. Dong, X. Li, Oxygen boost diffusion for the deep-case hardening of titanium alloys, Mater. Sci. Eng. A 280 (2000) 303–310.
[5] U. Diebold, The surface science of titanium dioxide, Surf. Sci. Rep. 48 (2003) 53–229.
[6] T.A. Wallace, R.K. Clark, K.E. Wiedemann, in: Oxidation Characteristics of Beta-21S in Air in the Temperature Range 600 to 800 °C, National Aeronautics and Space Administration, Langley Research Center, Hampton, VA, United States, 1992.
[7] I. Menzies, K. Strafford, The scaling of binary alloys of titanium containing 5 wt% of aluminium, copper, or cobalt in carbon dioxide at 1000 °C, J. Less Common Met. 12 (1967) 85–106.
[8] N. Cabrera, N. Mott, Theory of the oxidation of metals, Rep. Prog. Phys. 12 (1949) 163.
[9] P. Samimi, Y. Liu, I. Ghamarian, P.C. Collins, A novel tool to assess the influence of alloy composition on the oxidation behavior and concurrent oxygen-induced phase transformations for binary Ti–*x*Mo alloys at 650 °C, Corros. Sci. 89 (2014) 295–306.
[10] A.M. Chaze, C. Coddet, Influence of chromium on the oxidation of titanium between 550 °C and 700 °C, Oxid. Met. 21 (1984) 205–231.
[11] I. Menzies, K. Strafford, A kinetic and morphological study of the oxidation of Ti–Cr alloys in CO_2 at 1000 °C, Corros. Sci. 7 (1967) 23–38.
[12] D.J. McPherson, M.G. Fontana, Preparation and properties of titanium–chromium binary alloys, ASM Trans. 43 (1951) 27.
[13] Y. Shida, H. Anada, The influence of ternary element addition on the oxidation behaviour of TiAl intermetallic compound in high temperature air, Corros. Sci. 35 (1993) 945–953.
[14] Y. Shida, H. Anada, The effect of various ternary additives on the oxidation behavior of TiAl in high-temperature air, Oxid. Met. 45 (1996) 197–219.
[15] S. Becker, A. Rahmel, M. Schorr, M. Schütze, Mechanism of isothermal oxidation of the intel-metallic TiAl and of TiAl alloys, Oxid. Met. 38 (1992) 425–464.
[16] W. Kinna, W. Knorr, "Uber die Oxidation von Titan" (oxidation of titanium), Metallkunde 47 (1956) 4.
[17] C. Wagner, Beitrag zur Theorie des Anlaufvorganges, Zeitschrift of Physical Chemistry B 21 (1933) 25.
[18] L. Kaufman, H. Bernstein, Computer Calculation of Phase Diagrams with Special Reference to Refractory Metals, Academic Press, New York, 1970.
[19] N. Saunders, A.P. Miodownik, CALPHAD (Calculation of Phase Diagrams): A Comprehensive Guide: A Comprehensive Guide, Elsevier Science, 1998.
[20] G. Welsch, R. Boyer, E.W. Collings, Materials Properties Handbook: Titanium Alloys, ASM International, 1993.
[21] S. 1Banerjee, P. Mukhopadhyay, Phase Transformations: Examples from Titanium and Zirconium Alloys, Elsevier Science, 2010.
[22] C.A. Luke, R. Taggart, D.H. Polonis, The metastable constitution of quenched titanium and zirconium-base binary alloys, Trans. ASM 57 (1964) 142–149.
[23] E.K. Molchanova, in: Phase Diagrams of Titanium Alloys, IPST, 1965.
[24] G.H. Narayanan, T.S. Luhman, T.F. Archbold, R. Taggart, D.H. Polonis, A phase separation reaction in a binary titanium–chromium alloy, Metallography 4 (1971) 343–358.
[25] T. Luhman, R. Taggart, D. Polonis, Correlation of superconducting properties with the beta to omega phase transformation in Ti–Cr alloys, Scr. Metall. 3 (1969) 777–782.
[26] A.I.H. Committee, Alloy Phase Diagrams, ASM International, 1992.
[27] J.L. Murray, The Cr–Ti (chromium–titanium) system, Bull. Alloy Phase Diagrams 2 (1981) 174–181.
[28] A. Goldenstein, A. Metcalfe, W. Rostoker, The effect of stress on the eutectoid decomposition of titanium–chromium alloys, Trans. ASM 51 (1959) 1036–1053.

[29] P.C. Collins, B. Welk, T. Searles, J. Tiley, J.C. Russ, H.L. Fraser, Development of methods for the quantification of microstructural features in α + β-processed α/β titanium alloys, Mater. Sci. Eng. A 508 (2009) 174–182.
[30] H. Aaronson, W. Triplett, G. Andes, in: Effects of Composition on Transformations in Titanium–Chromium Alloys, Minerals Metals Materials Society, Warrendale, PA, 1958, pp. 624–626.
[31] H. Aaronson, W. Triplett, G. Andes, Phase transformations in hypoeutectoid Ti–Cr alloys, Trans. Am. Inst. Mining Metall. Eng. 209 (1957) 1227–1235.
[32] H. Aaronson, W. Triplett, G. Andes, Transformation mechanisms in a hypereutectoid titanium–chromium alloy, Trans. Am. Inst. Mining Metall. Eng. 218 (1960) 331–339.
[33] G.W. Franti, J.C. Williams, H.I. Aaronson, A survey of eutectoid decomposition in ten Ti–X systems, Metall. Trans. A 9 (1978) 1641–1649.
[34] H.J. Lee, H.I. Aaronson, Eutectoid decomposition mechanisms in hypoeutectoid Ti–X alloys, J. Mater. Sci. 23 (1988) 150–160.
[35] P. Kofstad, P. Anderson, O. Krudtaa, Oxidation of titanium in the temperature range 800–1200 °C, J. Less Common Met. 3 (1961) 89–97.
[36] P. Kofstad, K. Hauffe, H. Kjollesdal, Investigation on the oxidation mechanism of titanium, Acta Chem. Scand. 12 (1958) 239–266.
[37] N. Birks, G.H. Meier, F.S. Pettit, Introduction to the High Temperature Oxidation of Metals, Cambridge University Press, 2006.
[38] C. Rosa, Oxygen diffusion in alpha and beta titanium in the temperature range of 932–1142 °C, Metall. Trans. 1 (1970) 2517–2522.
[39] I. Gurappa, Protection of titanium alloy components against high temperature corrosion, Mater. Sci. Eng. A 356 (2003) 372–380.
[40] R.N. Shenoy, J. Unnam, R.K. Clark, Oxidation and embrittlement of Ti–6Al–2Sn–4Zr–2Mo alloy, Oxid. Met. 26 (1986) 105–124.
[41] T. Smith, Oxidation of titanium between 25 °C and 400 °C, Surf. Sci. 38 (1973) 292–312.
[42] M. Maruyama, S. Nakamura, S. Suenaga, M. Nakahashi, Formation process of Ti_3Al in Ti/Al_2O_3 system, MRS Online Proc. Libr. 458 (1996).
[43] A. Atkinson, Transport processes during the growth of oxide films at elevated temperature, Rev. Mod. Phys. 57 (1985) 437–470.
[44] Z. Xu, K.M. Rosso, S. Bruemmer, Metal oxidation kinetics and the transition from thin to thick films, PCCP 14 (2012) 14534–14539.
[45] F. Millot, C. Picard, Oxygen self-diffusion in non-stoichiometric rutile TiO_{2-x} at high temperature, Solid State Ionics 28–30 (Part 2) (1988) 1344–1348.
[46] M. Arita, M. Hosoya, M. Kobayashi, M. Someno, Depth profile measurement by secondary ion mass spectrometry for determining the tracer diffusivity of oxygen in rutile, J. Am. Ceram. Soc. 62 (1979) 443–446.
[47] P. Kofstad, Nonstoichiometry, Diffusion, and Electrical Conductivity in Binary Metal Oxides, Wiley-Interscience, 1972.
[48] R.t. Shannon, Revised effective ionic radii and systematic studies of interatomic distances in halides and chalcogenides, Acta Crystallogr., Sect. A: Cryst. Phys. Diffr. Theor. Gen. Crystallogr. 32 (1976) 751–767.
[49] A. Escudero, F. Langenhorst, Chromium incorporation into TiO_2 at high pressure, J. Solid State Chem. 190 (2012) 61–67.